Electronic Supplementary Information for

An alternating copolymer of phenothiazine and ethylenedioxythiophene for perovskite solar cells: effects of flexible and rigid substituent alternation

Bing Zhang,‡ Yaohang Cai,‡ Lifei He,‡ Niansheng Xu,* Yi Yuan, Jing Zhang, Yuyan Zhang* and Peng Wang*

State Key Laboratory of Silicon and Advanced Semiconductor Materials, Department of Chemistry, Zhejiang University, Hangzhou 310058, China

E-mail: nshxu@zju.edu.cn; yuyanzhang@zju.edu.cn; pw2015@zju.edu.cn

1. Experimental section

1.1. Materials

3,4-Ethylenedioxythiophene (EDOT, 98%, Bidepharm), tris(dibenzylideneacetone)dipalladium ($Pd_2(dba)_3$, 98%, Energy Chemical), tris(3-methoxyphenyl)phosphine (P(*o*-MeOPh)$_3$, 98%, Energy Chemical), *N*,*N*,*N*',*N*'-tetramethylethylenediamine (TMEDA, 99%, Energy Chemical), pivalic acid (PivOH, 99%, Energy Chemical), cesium carbonate (Cs_2CO_3, 99.9%, Energy Chemical), disodium dihydrogen ethylenediaminetetraacetate dihydrate (EDTA, 99%, Energy Chemical), 1-ethyl-3-methylimidazolium bis(trifluoromethanesulfonyl)imide (EMITFSI, 98%, Energy Chemical), ferrocene (97%, Aldrich), PEDOT:PSS (AI 4083, Heraeus® Clevios), benzocyclobutene (BCB, 98%, Energy Chemical), lead(II) iodide(PbI_2, 99.99%, TCI), rubidium chloride (RbCl, 99.9%, 3A), formamidinium iodide (FAI, 99.0%, Greatcell Solar), methylamine hydrochloride (MACl, 98%, TCI), triphenylmethane-4,4',4''-triisocyanate (TTI, 20% solution in chlorobenzene, Aladdin), polystyrene (PS, typical M_w ~ 280,000, Sigma-Aldrich), tin(IV) oxide (SnO_2, 15% hydrocolloid dispersion, Alfa Aesar), 4-*tert*-butylpyridine (TBP, 96%, Sigma-Aldrich), and *N*^{2},*N*^{2},*N*$^{2'}$,*N*$^{2'}$,*N*^{7},*N*^{7},*N*$^{7'}$,*N*$^{7'}$-octakis(4-methoxyphenyl)-9,9'-spirobi[fluorene]-2,2',7,7'-tetraamine (spiro-OMeTAD, 99.8%, Xi'an Polymer Light Technology Corp.) were obtained from commercial suppliers and used without further purification. Solvents including toluene (≥ 99.5%, Sinopharm Chemical Reagent Co., Ltd.), tetrahydrofuran (THF, ≥ 99%, Sinopharm Chemical Reagent Co., Ltd.), methanol (≥ 99.5%, Sinopharm Chemical Reagent Co., Ltd.), deuterated tetrahydrofuran (THF-d_8, 99%, J&K Scientific), acetonitrile (MeCN, ≥ 99.9%, Energy Chemical), acetone (≥ 99.5%, Sinopharm Chemical Reagent Co., Ltd), ethanol (99.7%, Aladdin), chlorobenzene (99.8%, Acros Organics), dimethyl sulfoxide (DMSO, 99.9%, Sigma-Aldrich), *N*,*N*-dimethylformamide (DMF, Water ≤ 30 ppm, 99.9%, Energy Chemical), and 2-propanol (IPA, 99.5%, Sigma-Aldrich) were also procured from commercial sources and employed without further purification. Deionized water with resistivity greater than 18 MΩ cm was provided by a UPR-II-10T Ultrapure water system (ULUPURE). 3,7-Dibromo-10-(2-octyldodecyl)-10*H*-phenothiazine (2Br-PTZOD),[1] 3,7-dibromo-10-mesityl-10*H*-phenothiazine(2Br-PTZMes),[2] 3,7-bis(2,3-dihydrothieno[3,4-*b*][1,4]dioxin-5-yl)-10-(2-octyldodecyl)-10*H*-phenothiazine (E-PTZOD-E),[3] 4-(*tert*-butyl)pyridinium 1,1,2,2,3,3-hexafluoropropane-1,3-disulfonimide (TBPH-HFSI),[4] and 4-(*tert*-butyl)pyridinium bis(trifluoromethanesulfonyl)imide (TBPH-TFSI)[5] were prepared according to literature methods.

1.2. General instrumentation

Melting point determinations were conducted using a WRS-1B digital melting point apparatus (INESA). ^{1}H nuclear magnetic resonance (NMR) spectra were acquired on an AVANCE III 400 NMR spectrometer (Bruker). All chemical shifts were referenced to THF-d_8. Attenuated total reflection-Fourier transform infrared (ATR-FTIR) spectroscopy measurements were carried out utilizing a Thermo Scientific™ Nicolet™ iS50 FTIR spectrometer. Ultraviolet-visible (UV-vis) absorption spectra were acquired with a Cary 8454 spectrophotometer (Agilent Technologies). Carbon, hydrogen, and nitrogen content analyses were conducted employing a Vario Micro cube element analyzer (Elementar Analysensysteme GmbH). High temperature gel permeation chromatography (HT-GPC) measurements were performed using a PL-GPC220 instrument (Polymer Laboratories Ltd.), with 1,2,4-trichlorobenzene as the eluent. Differential scanning calorimetry measurements were executed on a DSC Q100 V9.7 Build 291 instrument (TA) under a flowing nitrogen atmosphere, employing a heating rate of 10 ^{o}C min^{-1}. Atom force microscopy measurements were conducted by a Park NX10 microscope (Park Systems). Top-view surface morphology of a thin film was imaged using a SU-70 field emission scanning electron microscope (Hitachi). Fluorescence optical microscopy images were recorded employing an ECLIPSE Ti-U system (Nikon).

1.3. Synthesis

1.3.1. p-PTZOD-E

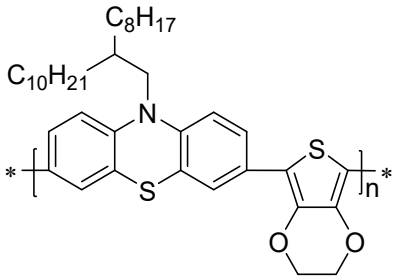

In a dried Schlenk tube, 2Br-PTZOD (1.28 g, 2.0 mmol), EDOT (284 mg, 2.0 mmol), $Pd_2(dba)_3$ (92 mg, 0.10 mmol), P(*o*-MeOPh)$_3$ (141 mg, 0.40 mmol), TMEDA (116 mg, 1.00 mmol), PivOH (1.02 g, 10.00 mmol), Cs_2CO_3 (3.26 g, 10.00 mmol), and toluene (40 mL) were introduced. The tube was then evacuated and purged with argon for three times. The reaction mixture was stirred at 110 °C under an argon atmosphere for 16 hours. Upon cooling to room temperature, the solvent was removed using a rotary evaporator, and methanol (20 mL) was introduced. The solids were collected via filtration, followed by successive washing with a 0.1 M EDTA aqueous solution, water, and methanol. The residue was subjected to purification on a silica gel column using eluents of toluene/petroleum ether 60–90°C (*v*/*v*, 1/1) and toluene/THF (*v*/*v*, 1/1) sequentially. The toluene/THF fraction was collected, concentrated to a small volume, and added dropwise to methanol (200 mL). After filtration and drying, the desired product was obtained as a yellow powder (1.3 g, 83% yield). Melting point: > 300 °C. ^{1}H NMR (400 MHz, THF-d_8) δ: 7.54–7.27 (m, 4H), 6.89–6.76 (m, 2H), 4.31–4.19 (m, 4H), 3.77–3.63 (m, 2H), 1.95–1.86 (br, 1H), 1.36–1.08 (m, 32H), and 0.80–0.74 (m, 6H) ppm. ATR-FTIR (film) ν_{max}: 2919, 2850, 1464, 1356, 1253, 1085, 1032, 808, and 725 cm^{-1}. UV-vis (THF) λ_{max}: 332 and 430 nm. Elemental analysis calcd. for $(C_{38}H_{51}NO_2S_2)_n$: C, 73.86; H, 8.32; N, 2.27. Found: C, 73.88; H, 8.35; N, 2.31.

1.3.2. p-PTZMes-E

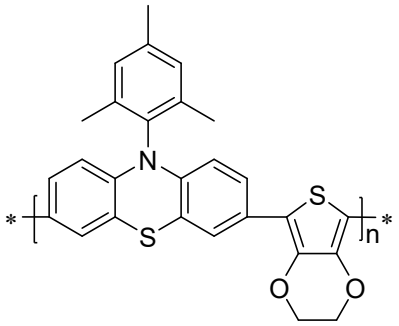

In a dried Schlenk tube, 2Br-PTZMes (950 mg, 2.0 mmol), EDOT (284 mg, 2.0 mmol), $Pd_2(dba)_3$ (92 mg, 0.10 mmol), P(*o*-MeOPh)$_3$ (141 mg, 0.40 mmol), TMEDA (116 mg, 1.00 mmol), PivOH (1.02 g, 10.00 mmol), Cs_2CO_3 (3.26 g, 10.00 mmol), and toluene (40 mL) were introduced. The tube was then evacuated and purged with argon for three times. The reaction mixture was stirred at 110 °C under an argon atmosphere for 16 hours. Upon cooling to room temperature, the solvent was removed using a rotary evaporator, and methanol (20 mL) was introduced. The solids were collected via filtration, followed by successive washing with a 0.1 M EDTA aqueous solution, water, and methanol. The residue was subjected to purification on a silica gel column using eluents of toluene/ petroleum ether 60–90°C (*v*/*v*, 1/1) and toluene/THF (*v*/*v*, 1/1) sequentially. The toluene/THF fraction was collected, concentrated to a small volume, and added dropwise to methanol (200 mL). After filtration and drying, the desired product was obtained as an orange powder (675 mg, 74% yield). Melting point: > 300 °C. ^{1}H NMR (400 MHz, THF-d_8) δ: 7.46–6.83 (m, 6H), 5.82–5.64 (m, 2H), 4.27–4.04 (m, 4H), 2.32–2.18 (m, 3H), and 2.15–1.94 (m, 6H)

ppm. ATR-FTIR (film) ν_{max}: 2918, 1468, 1359, 1308, 1254, 1090, 856, 809, and 713 cm^{-1}. UV-vis (THF) λ_{max}: 343 and 473 nm. Elemental analysis calcd. for $(C_{27}H_{21}NO_2S_2)_n$: C, 71.18; H, 4.65; N, 3.07. Found: C, 71.23; H, 4.62; N, 3.09.

1.3.3. p-PTZMes-E-PTZOD-E

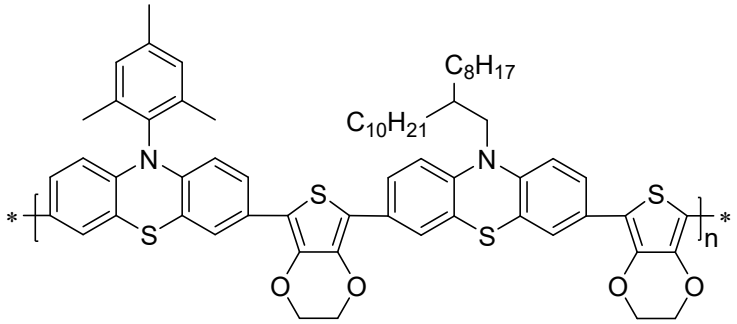

In a dried Schlenk tube, 2Br-PTZMes (950 mg, 2.0 mmol), E-PTZOD-E (1.52 g, 2.0 mmol), $Pd_2(dba)_3$ (92 mg, 0.10 mmol), P(*o*-MeOPh)$_3$ (141 mg, 0.40 mmol), TMEDA (116 mg, 1.00 mmol), PivOH (1.02 g, 10.00 mmol), Cs_2CO_3 (3.26 g, 10.00 mmol), and toluene (40 mL) were introduced. The tube was then evacuated and purged with argon for three times. The reaction mixture was stirred at 110 °C under an argon atmosphere for 16 hours. Upon cooling to room temperature, the solvent was removed using a rotary evaporator, and methanol (20 mL) was introduced. The solids were collected via filtration, followed by successive washing with a 0.1 M EDTA aqueous solution, water, and methanol. The residue was subjected to purification on a silica gel column using eluents of toluene and toluene/THF (*v*/*v*, 1/1) sequentially. The toluene/THF fraction was collected, concentrated to a small volume, and added dropwise to methanol (200 mL). After filtration and drying, the desired product was obtained as a yellow powder (1.8 g, 84% yield). Melting point: > 300 °C. ^{1}H NMR (400 MHz, THF-d_8) δ: 7.46–7.33 (m, 4H), 7.26–7.15 (m, 2H), 7.05–6.98 (m, 4H), 6.84–6.78 (m, 2H), 5.79–5.70 (m, 2H), 4.27–4.16 (m, 8H), 3.75–3.64 (m, 2H), 2.29–2.24 (m, 3H), 2.09–2.03 (m, 6H), 1.93–1.86 (br, 1H), 1.33–1.10 (m, 32H), and 0.80–0.73 (m, 6H) ppm. ATR-FTIR (film) ν_{max}: 2921, 2851, 1469, 1358, 1313, 1255, 1089, 856, 810, and 713 cm^{-1}. UV-vis (THF) λ_{max}: 337 and 454 nm. Elemental analysis calcd. for $(C_{65}H_{72}N_2O_4S_4)_n$: C, 72.72; H, 6.76; N, 2.61. Found: C, 72.76; H, 6.79; N, 2.65.

1.4. Cyclic voltammetry measurements

Cyclic voltammograms were recorded using a CHI660E electrochemical workstation (CH Instruments). A 10 μL solution of polymeric semiconductor in chlorobenzene, with a concentration of 5 mg mL^{-1}, was drop-cast onto the pre-cleaned surface of a 3 mm diameter glassy carbon electrode and air-dried, resulting in a modified working electrode. The electrolytic cell consisted of the modified working electrode, a fluorine-doped tin oxide counter electrode, and an Ag/AgCl (sat. KCl) reference electrode. EMITFSI (0.1 M in MeCN) served as the supporting electrolyte. The scan rate was set at 50 mV s^{-1}. All potentials are reported with ferrocene as reference.

1.5. Ultraviolet photoelectron spectroscopy (UPS) measurements

Indium-doped tin oxide (ITO) glass substrates (12 Ω sq^{-1}, 1.6 mm thickness) underwent sequential sonication in detergent, deionized water, acetone, and ethanol for 15 minutes each. Subsequently, UV-ozone treatment was applied to activate the surface for 15 minutes. A uniform layer of PEDOT:PSS was spin-coated at 3000 rpm for 30 seconds onto the prepared ITO substrate and annealed at 150°C for 30 minutes. After cooling to room temperature, a polymeric semiconductor layer was deposited via spin-coating at 3000 rpm for 30 seconds using a chlorobenzene solution containing either p-PTZOD-E, p-PTZMes-E or p-PTZMes-E-PTZOD-E dissolved at a concentration of 20 mg mL^{-1}. UPS spectra were recorded using an ESCALAB XI+ instrument (Thermo Fisher).

1.6. Hole extraction

1.6.1. Sample preparation

The glass slides underwent sequential sonication in detergent, deionized water, acetone, and ethanol for 15 minutes each. Following cleaning, the glass slides were treated with UV-ozone for 15 minutes and then transferred into a glove box filled with dry air (< 3% relative humidity). The fabrication of the $FAPbI_3$ perovskite layer involved a two-step spin-coating process. Initially, a solution containing 1.5 M PbI_2 and 7.5 mM RbCl in a DMF:DMSO solvent mixture (9:1 volume ratio) was spin-coated onto the cleaned glass slides at 1500 rpm for 30 seconds, followed by annealing at 70°C for 1 minute. Subsequently, a solution mixture of FAI:MACl (90 mg:13.5 mg in 1 mL IPA) was spin-coated onto the PbI_2 layer at 1800 rpm for 30 seconds. The resulting film was annealed at 150°C for 30 minutes, resulting in the formation of the $FAPbI_3$ perovskite layer, incorporating a minor quantity of $(PbI_2)_2RbCl$.[6] For the passivation layer, a TTI-derived interlayer (2.5 mg mL^{-1} in chlorobenzene) was spin-coated at 5000 rpm for 30 seconds and annealed at 85°C for 20 minutes.[4] Subsequently, a chlorobenzene solution contained p-PTZOD-E (50 mg mL^{-1}), p-PTZMes-E (50 mg mL^{-1}), p-PTZMes-E-PTZOD-E (50 mg mL^{-1}), spiro-OMeTAD (50 mg mL^{-1}), or polystyrene (50 mg mL^{-1}) was spin-coated at 5000 rpm for 30 seconds.

1.6.2. Time-resolved photoluminescence measurements

Time-resolved photoluminescence decay measurements were conducted using a Life-Spec-II fluorescence spectrometer (Edinburgh Instruments).

1.7. Direct-current conductivity measurements

The direct-current conductivities (σ) of both pristine and composite organic semiconductor films, deposited onto interdigital gold electrodes comprising 119 channels (n), each with a channel length (L) of 1.5 mm, a channel width (W) of 10 μm, and a channel thickness (t) of 110 nm, were determined by obtaining current–voltage (I–V) curves across potential biases ranging from −1.0 V to 1.0 V. An organic semiconductor layer was spin-coated from a chlorobenzene solution containing p-PTZOD-E (50 mg mL^{-1}), p-PTZMes-E (50 mg mL^{-1}), p-PTZMes-E-PTZOD-E (50 mg mL^{-1}), or spiro-OMeTAD (50 mg mL^{-1}), each in combination with 132 mM TBP and varying weight percentages of TBPH-HFSI (0%, 5%, 10%, or 15%), at 3000 rpm for 30 seconds. Prior to measurement, the devices were stored in a dry air environment (< 5% relative humidity) for 7 days. I–V measurements were conducted using a Keithley 2400 source meter, with test automation facilitated by Labview 14.0. The calculation of σ was performed using the formula $\sigma = sW/nLt$, where s represents the slope obtained from linear fitting of the I–V plot.

1.8. Hole density measurements

1.8.1. Pristine films

To quantify the hole density (p) of pristine organic semiconductors, we performed impedance spectroscopy measurements on metal-insulator-semiconductor (MIS) devices. The MIS device architecture consisted of layers of n^{++}-Si/SiO_2/p-BCB/organic semiconductor/Au. The p-BCB layer was formed through a spin-coating process at 4000 rpm for 30 seconds using a BCB chlorobenzene solution (1 mg mL^{-1}), followed by annealing at 250°C for 1 hour. Subsequently, an organic semiconductor layer was spin-coated from a chlorobenzene solution containing 132 mM TBP and p-PTZOD-E (50 mg mL^{-1}), p-PTZMes-E (50 mg mL^{-1}), p-PTZMes-E-PTZOD-E (50 mg mL^{-1}), or spiro-OMeTAD (50 mg mL^{-1}) at 3000 rpm for 30 seconds, followed by the thermal evaporation of gold contacts (approximately 100 nm). Impedance spectra were acquired using an Autolab PGSTAT302N electrochemical workstation (Metrohm), covering a wide frequency range (10 Hz–3 MHz) with a small perturbation of 20 mV. The capacitance (C) was calculated using the equation: $C = -\frac{1}{\omega}\left[\frac{Z'' - \omega L_i}{(Z' - R_s)^2 + (Z'' - \omega L_i)^2}\right]$, where ω denotes the angular frequency, Z' and Z'' represent the real and imaginary components of impedance, R_s is the series resistance, and L_i denotes the parasitic inductance. The p value was extracted from the slope of the Mott-Schottky plot, given by:

$p = \frac{2}{q\varepsilon_r\varepsilon_0 \frac{\mathrm{d}(A/C)^2}{\mathrm{d}V}}$, where q is the elementary charge, ε_r denotes the relative permittivity, ε_0 signifies the vacuum permittivity, and A represents the area of the MIS device.

1.8.2. Composite films

The determination of p for an organic semiconductor film containing TBPH-HFSI presented a challenge. To address this obstacle, we adopted a comparative approach based on the quadratic integral intensities of electron paramagnetic resonance (EPR) signals originating from organic semiconductor films with and without TBPH-HFSI. The established p value for a pristine organic semiconductor film served as the reference for this estimation. To capture the EPR spectrum, we applied a chlorobenzene solution onto a 2 cm × 2 cm microslide using the drop-casting method, subsequently crushed the microslide, and transferred it into a borosilicate glass tube. The chlorobenzene solutions were formulated to contain p-PTZOD-E (50 mg mL^{-1}), p-PTZMes-E (50 mg mL^{-1}), p-PTZMes-E-PTZOD-E (50 mg mL^{-1}), or spiro-OMeTAD (50 mg mL^{-1}), each in combination with 132 mM TBP and varying weight percentages of TBPH-HFSI (5%, 10%, or 15%). EPR measurements were performed using an A300-10/12 spectrometer (Bruker).

1.9. Perovskite solar cells

1.9.1. Fabrication

The cleaned ITO substrates underwent UV-ozone treatment for 15 minutes prior to use. A diluted SnO_2 colloid dispersion, with a deionized water ratio of 1:4, was then subjected to filtration through a 0.2 μm PTFE filter. Subsequently, this refined solution was spin-coated onto the pristine ITO substrate at 4000 rpm for 30 seconds, followed by annealing at 150°C for 30 minutes within an ambient air environment.[7] Following UV-ozone treatment, the glass/ITO/SnO_2 substrates were transferred into a glove box filled with dry air (<3% relative humidity) for the deposition of perovskite layer, TTI-derived interlayer, and hole transport layer as described in Section 1.6.1. The chlorobenzene solution used for the deposition of the hole transport layer contained p-PTZOD-E (50 mg mL^{-1}), p-PTZMes-E (50 mg mL^{-1}), p-PTZMes-E-PTZOD-E (50 mg mL^{-1}), or spiro-OMeTAD (50 mg mL^{-1}), each in conjunction with 15 wt% TBPH-HFSI and 132 mM TBP. Finally, a gold electrode (~ 100 nm) was deposited using a shadow mask under a vacuum of ≤ 1×10^{-4} Pa. The resulting device, with an active area of 0.10 cm^2 was laminated with a high-quality anti-reflective film on the glass side. Next, the cell was covered with waterproof adhesive tape on the gold electrode side, further sealed with an epoxy adhesive (3M), and stored in dry air overnight.

1.9.2. Optoelectronic measurements

The current density–voltage characteristics were determined using a Keithley 2400 source meter, with test automation facilitated by LabVIEW 14.0. Incident illumination was provided by an LS1000-4S-AM solar simulator (Solar Light Company), delivering AM1.5G irradiation level at 100 mW cm^{-2}, the intensity of which was validated via calibration against a silicon solar cell. To precisely define the photoactive region, a black metal mask with an aperture area of 0.07 cm^2 was utilized. The devices underwent comprehensive examination through both reverse scans (1.2 V → –0.1 V, incrementing in 0.005 V steps) and forward scans (–0.1 V → 1.2 V, with the same incremental step), conducted at a scan rate of 50 mV s^{-1}. For external quantum efficiency measurements, an Omni-λ300 monochromator (Zolix, China) and a 150 W xenon lamp (Zolix, China) was employed. The photocurrent data were recorded using a Keithley 2400 source meter. In quantifying the monochromatic light intensity, a Hamamatsu S1337-1010BQ silicon diode calibrated at the National Institute of Metrology, China, was employed. In the context of LED operation, measurements occurred within a nitrogen-filled glovebox at room temperature. For the assessment of external quantum efficiency of electroluminescence (EQE_{EL}), a custom setup was deployed, featuring a Keithley 2400 source meter, an integration sphere (FOIS-1), and a QE Pro spectrometer.

1.9.3. Storage stability at 85 °C

To evaluate the dark storage stability at 85°C (ISOS-D-2), perovskite solar cells were placed in an FD56 oven (Binder) set to the specified temperature. The atmospheric humidity surrounding the oven ranged from 45% to 90%. Periodic *J–V* measurements were conducted under AM1.5G conditions to continually monitor the performance parameters.

1.9.4. Operational stability at 45 °C

Maximum power point (MPP) tracking was conducted using a 16-channel photovoltaic tracking system from YH Electronic Equipment Business, coupled with the SLS-LED-80A solar simulator by Qingdao Solar Scientific Instrument High-tech Co., LTD. The experiment was performed in a nitrogen-filled glovebox to ensure controlled conditions. MPP data were gathered at 5-minute intervals utilizing the perturb and observe method.

1.9.5. Device dismantling

The dismantling process commenced with the meticulous removal of the epoxy adhesive and waterproof adhesive tape, resulting in partial detachment of the gold electrode. Subsequently, a layer of magic tape (Scotch, 3M) was affixed onto the residual gold layer. Upon careful removal of the magic tape, the gold layer was completely eradicated. In cases where required, the hole transport layers underwent additional cleansing through five cycles of dynamic spin-coating with chlorobenzene.

2. Theoretical modeling

2.1. Density functional theory calculation

The frontier molecular orbitals were calculated employing the Gaussian 16 program suite within the framework of periodic boundary condition−density functional theory or density functional theory at the B3LYP/6-311G(d,p) level. The frontier molecular orbitals were visualized via GaussView 5.0.

2.2. Molecular dynamics simulation

Polymer chains with a molecular weight of approximately 10 kDa were constructed using the Build Polymer tool in Material Studio 8.0. Subsequently, cubic boxes with periodic boundaries were generated using the Amorphous Cell module, accommodating 10 polymer chains. Molecular dynamics simulations were conducted employing the COMPASS II force field. Glass transition temperature and diffusivity investigations were carried out using the FORCITE module in Materials Studio 8.0. Our simulation protocol initiated with an initial NVT simulation at 700 K using a Nose thermostat, followed by an NPT simulation at 700 K utilizing both a Nose thermostat and a Berendsen barostat. Subsequently, a stepwise cooling process from 700 K down to 200 K was performed, with NVT and NPT simulations executed at each temperature. Specific volumes were recorded upon full equilibration at each temperature. The theoretical glass transition temperature was determined by intersection analysis of linear fitting lines in the low and high temperature regimes. The composites of organic semiconductor and salt were also modeled with TBPH-HFSI molecules at a weight percentage of 15. Furthermore, FAI was introduced into the composites, and NVT and NPT simulations were conducted. The mean square displacements of recorded trajectories were analyzed to unveil theoretical diffusivities.

3. Supplementary figures and tables

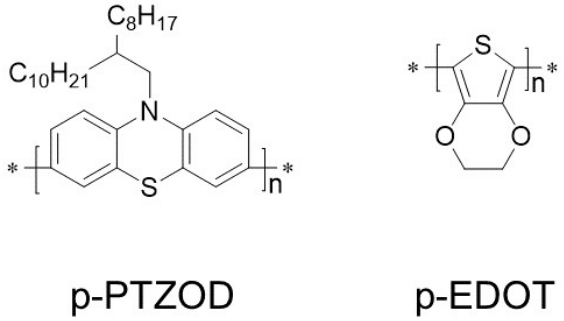

Fig. S1 Chemical structures of the homopolymer of 2-octyldodecyl-substituted phenothiazine (p-PTZOD) and the homopolymer of ethylenedioxythiophene (p-EDOT).

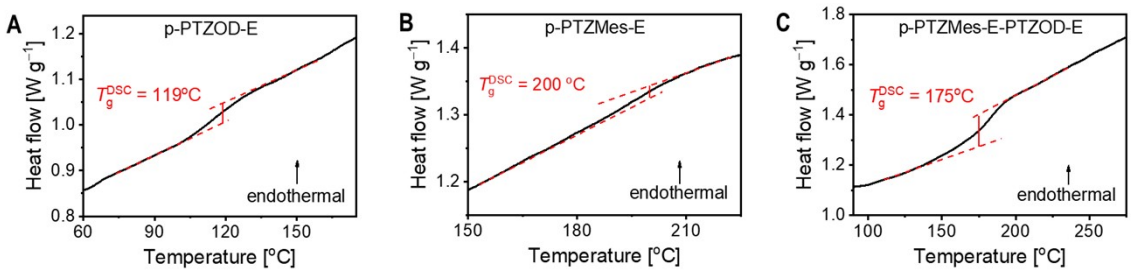

Fig. S2 Differential scanning calorimetry curves, with the glass transition temperature (T_g^{DSC}) indicated.

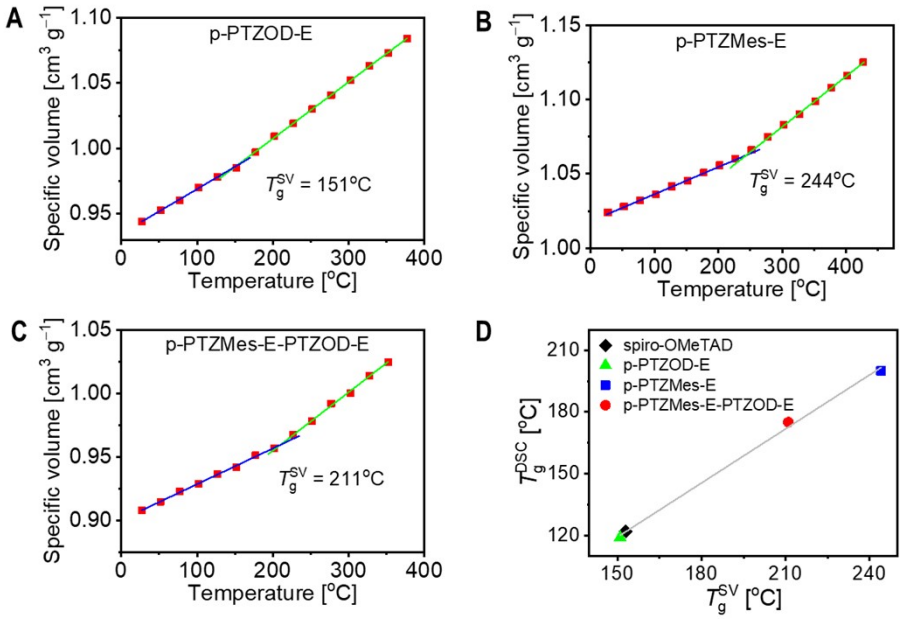

Fig. S3 (A–C) Specific volume as a function of temperature from molecular dynamics simulations. The blue and green solid lines represent linear fits for the low-temperature and high-temperature regions, respectively. The intersection of these lines corresponds to the theoretical glass transition temperature (T_g^{SV}). (D) Correlation between the glass transition temperature determined by differential scanning calorimetry (T_g^{DSC}) and T_g^{SV}. Data for spiro-OMeTAD are also included for comparison.[8]

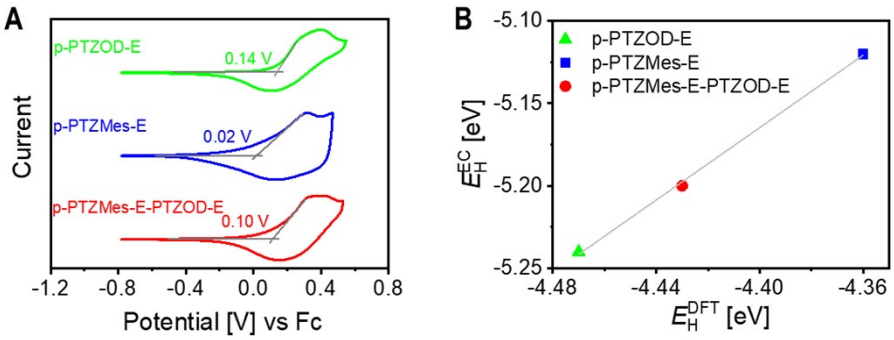

Fig. S4 (A) Thin-film cyclic voltammograms of three phenothiazine-ethylenedioxythiophene alternating copolymers. The intersection of the tangent to the oxidation wave and the baseline parallel to the x-axis defines the oxidation onset potential (V_{onset}), which is indicated for each polymer. The HOMO energy levels (E^{EC}_{H}) were calculated using the equation $E^{EC}_{H} = -5.10 - V_{onset}$.[9] The E^{EC}_{H} values for p-PTZOD-E, p-PTZMes-E, and p-PTZMes-E-PTZOD-E are −5.24 eV, −5.12 eV, and −5.20 eV, respectively. It should be noted that due to the relatively high solubility of spiro-OMeTAD in acetonitrile, a reliable thin-film cyclic voltammogram could not be obtained using this method. (B) Correlation between E^{EC}_{H} and the HOMO energy levels calculated by density functional theory (E^{DFT}_{H}).

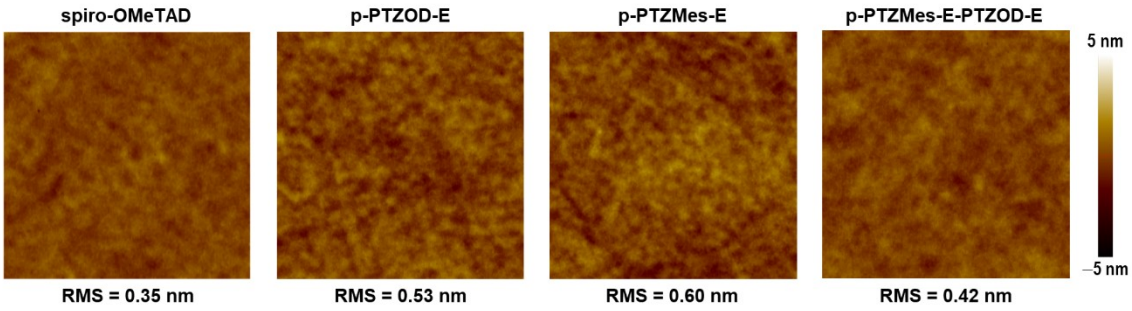

Fig. S5 Atomic force microscopy images of pristine organic semiconductor films spin-coated on PEDOT:PSS substrates. The root mean square (RMS) roughness values are shown below each image. Image size: 5 μm × 5 μm.

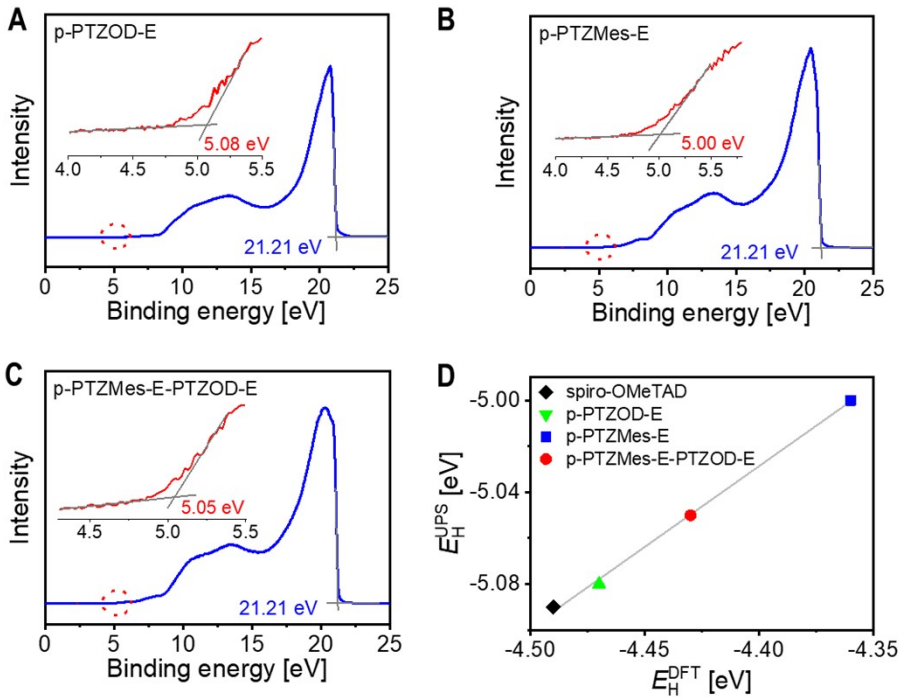

Fig. S6 (A–C) Ultraviolet photoelectron spectra of polymeric semiconductors spin-coated on ITO/PEDOT:PSS substrates. The spectra are calibrated using the cutoff energy corresponding to He I photon energy (21.21 eV). The inset shows an enlarged view of the onset region. The intersection of the tangent to the spectrum in the low binding energy region with the baseline parallel to the x-axis defines the HOMO energy level ($E^{\mathrm{UPS}}_{\mathrm{H}}$). (D) Correlation between $E^{\mathrm{UPS}}_{\mathrm{H}}$ and theoretically calculated HOMO energy level ($E^{\mathrm{DFT}}_{\mathrm{H}}$). Data for spiro-OMeTAD are also included for comparison.[10]

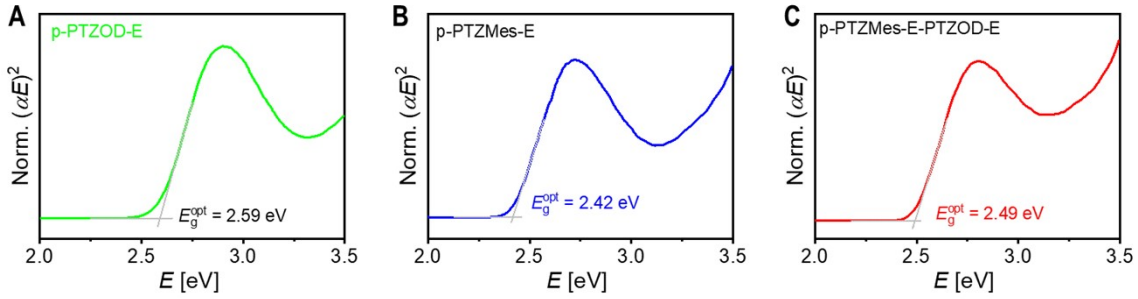

Fig. S7 (A–C) Tauc plots of polymeric semiconductors spin-coated on quartz substrates. Here, E, α, and $E^{\mathrm{opt}}_{\mathrm{g}}$ denote photon energy, optical absorption coefficient, and optical bandgap, respectively. The intersection of the tangent to the curve in the low-energy region with the baseline parallel to the x-axis determines $E^{\mathrm{opt}}_{\mathrm{g}}$.

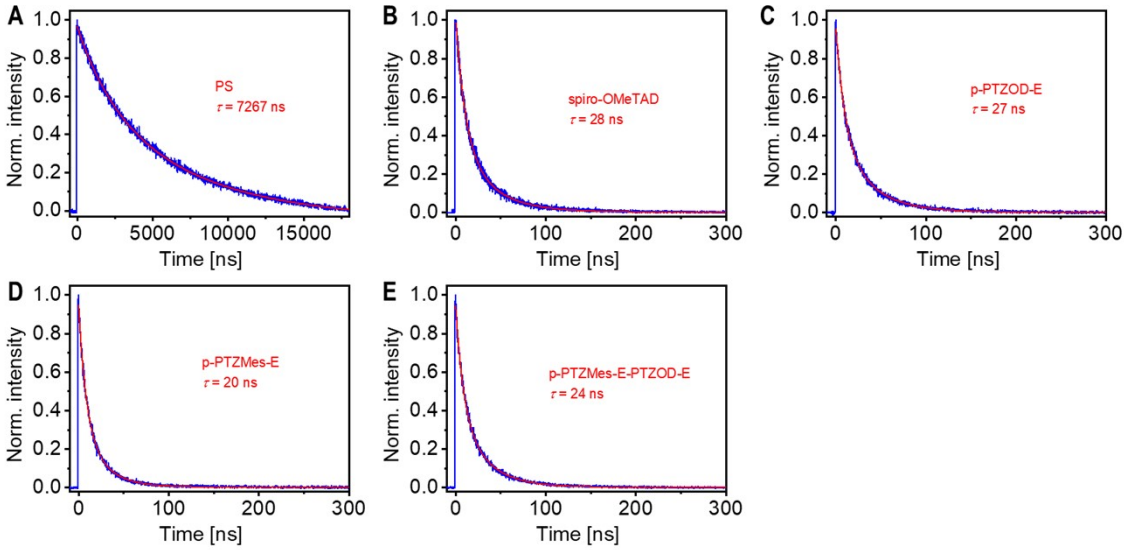

Fig. S8 (A–E) Time-resolved photoluminescence traces at 810 nm of TTI-modified $FAPbI_3$ films on glass substrates. The perovskite layer is overlaid with a thin film of polystyrene or organic semiconductor. The magenta curve represents a double-exponential decay fit, providing fitting parameters used to calculate the amplitude-weighted average photoluminescence lifetime (τ). Excitation wavelength: 670 nm.

Table S1. Fit parameters of photoluminescence decays for $FAPbI_3$ films coated with various organic layers on glass substrates, encompassing the amplitude-weighted average photoluminescence lifetime, hole extraction rate constant, and hole extraction yield[a]

Sample	τ_1 [ns]	A_1	τ_2 [ns]	A_2	τ [ns]	k_{he} [μs^{-1}]	ϕ_{he} [%]
glass/$FAPbI_3$/PS	2741.0	0.21	8469.6	0.79	7266.6	/	/
glass/$FAPbI_3$/spiro-OMeTAD	12.3	0.50	44.1	0.50	28.2	35.3	99.6
glass/$FAPbI_3$/p-PTZOD-E	10.0	0.32	35.2	0.68	27.1	36.8	99.6
glass/$FAPbI_3$/p-PTZMes-E	11.2	0.69	40.0	0.31	20.1	49.6	99.7
glass/$FAPbI_3$/p-PTZMes-E-PTZOD-E	9.9	0.35	31.5	0.65	23.9	41.7	99.7

[a] τ_1 and τ_2 represent the time constants of photoluminescence decay, A_1 and A_2 represent the relative amplitudes, and τ represents the amplitude-weighted average photoluminescence lifetime obtained by using equation $\tau = A_1\tau_1 + A_2\tau_2$. The hole extraction rate constant (k_{he}) is obtained by using equation $k_{he} = (\tau_{PS} - \tau_{OSC}) / (\tau_{PS} \times \tau_{OSC})$. ϕ_{he} represents the hole extraction yield obtained by using equation $\phi_{he} = (\tau_{PS} - \tau_{OSC}) / \tau_{PS}$ where τ_{PS} represents amplitude-weighted average photoluminescence lifetime of the glass-supported $FAPbI_3$ film covered with polystyrene (PS), and τ_{OSC} represents the amplitude-weighted average photoluminescence lifetime of the glass-supported $FAPbI_3$ film covered with organic semiconductors (OSC).

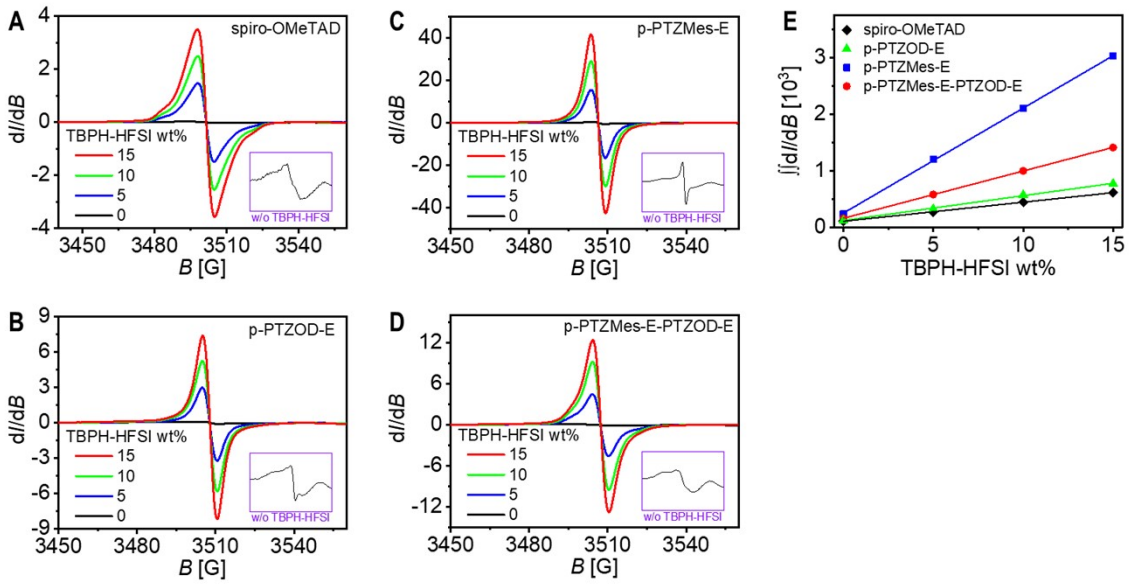

Fig. S9 (A–D) Electron paramagnetic resonance (EPR) spectra of organic semiconductor films containing varying TBPH-HFSI weight percentages (wt%). d*I*/d*B* represents the first derivative of absorption intensity (*I*), with *B* denoting the magnetic field strength. Even in the absence of TBPH-HFSI, the EPR signal is clearly observable in all pristine organic semiconductor samples (inset), suggesting inadvertent doping of the organic semiconductor films, likely by atmospheric oxygen, resulting in corresponding cationic radicals. As the weight percentage of the doping promoter TBPH-HFSI increases, the intensity of the EPR signal gradually strengthens. (E) Relationship between the quadratic integral of EPR signal ($\iint(dI/dB)$) and TBPH-HFSI wt%. The solid line depicts a linear fit, indicating that the apparent doping efficiency does not decrease with increasing salt content.

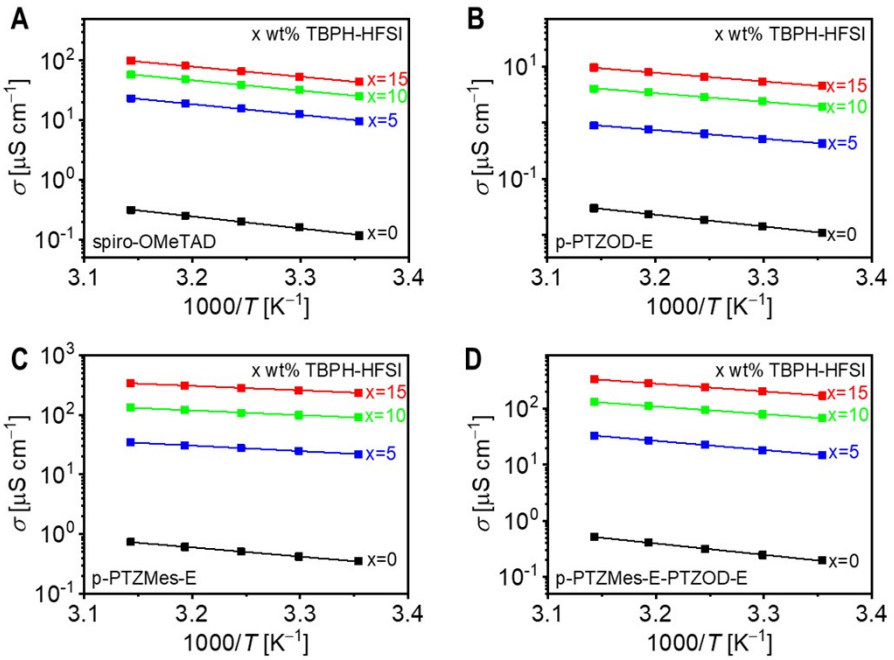

Fig. S10 (A–D) Arrhenius plots of the conductivity (σ) of organic semiconductor films: (A) spiro-OMeTAD; (B) p-PTZOD-E; (C) p-PTZMes-E; (D) p-PTZMes-E-PTZOD-E. Kelvin temperature is denoted by *T*.

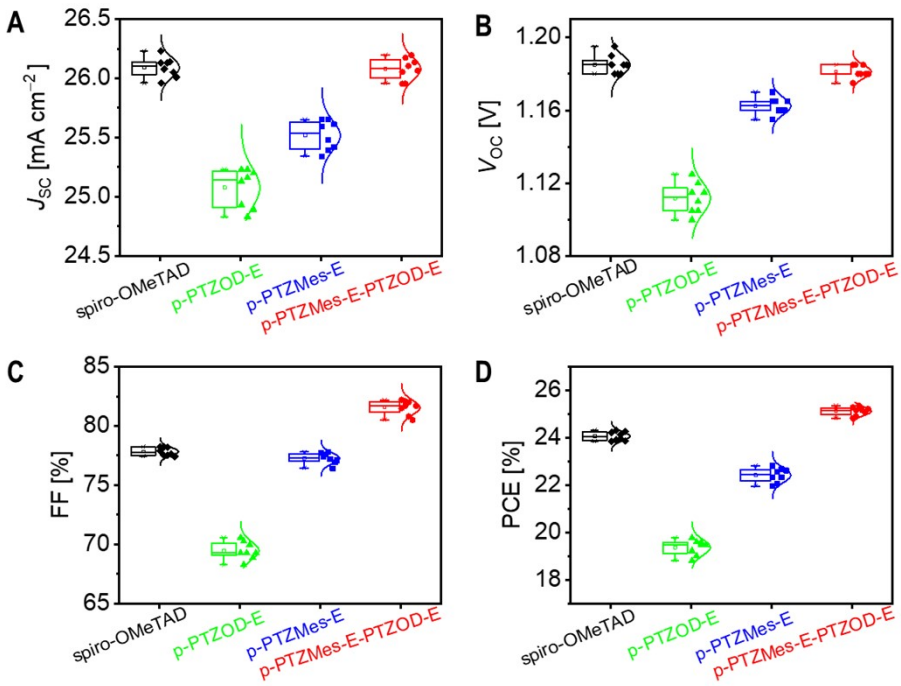

Fig. S11 (A–D) Photovoltaic parameter statistics for as-prepared perovskite solar cells employing various hole transport layers containing 15 wt% TBPH-HFSI, under AM1.5G simulated sunlight irradiation (100 mW cm^{-2}): (A) short-circuit current density (J_{SC}); (B) open-circuit voltage (V_{OC}); (C) fill factor (FF); (D) power conversion efficiency (PCE).

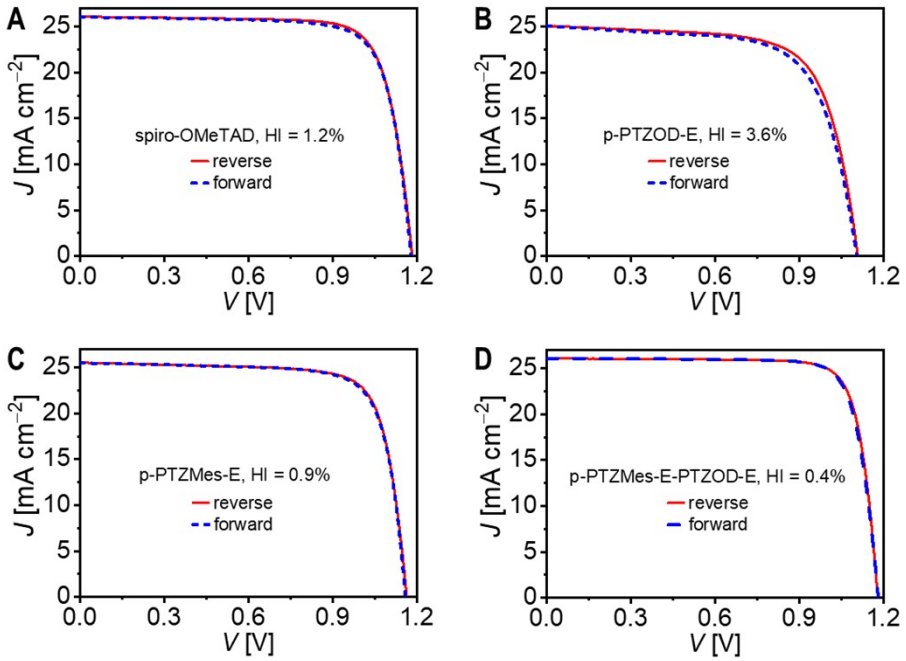

Fig. S12 (A–D) Representative forward and reverse photocurrent density–voltage (*J*–*V*) scans of as-prepared perovskite solar cells under AM1.5G illumination at 100 mW cm^{-2}. The hysteresis index (HI) is calculated as ($PCE_{reverse}$ – $PCE_{forward}$) / $PCE_{reverse}$.

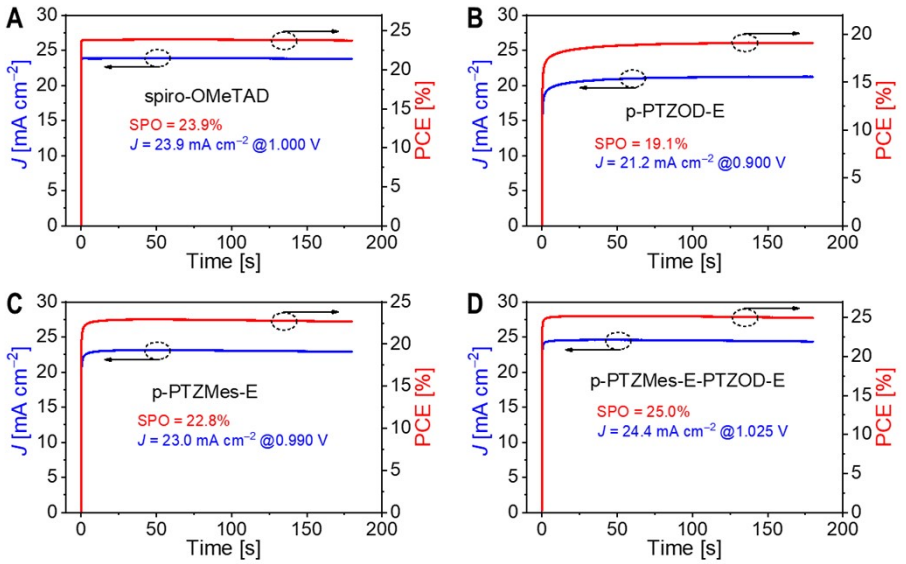

Fig. S13 (A–D) Representative steady-state photocurrent density (*J*) and power conversion efficiency (PCE) outputs of as-prepared perovskite solar cells under AM1.5G illumination at 100 mW cm^{-2}.

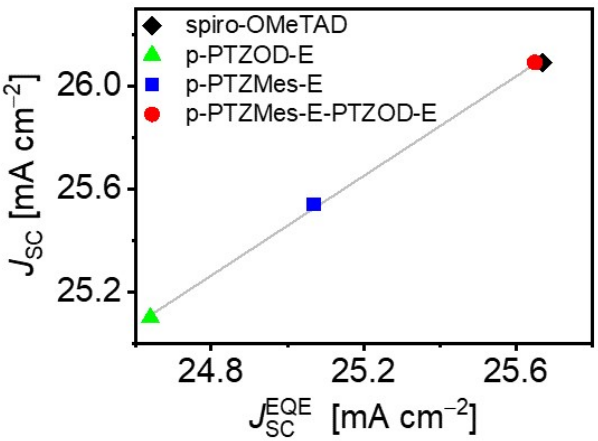

Fig. S14 Relationship between short-circuit photocurrent density from *J*–*V* measurements (J_{SC}) of as-prepared perovskite solar cells with various hole transporting layers and short-circuit photocurrent density derived from external quantum efficiency spectra (J_{SC}^{EQE}). The gray line represents a linear fit to the data.

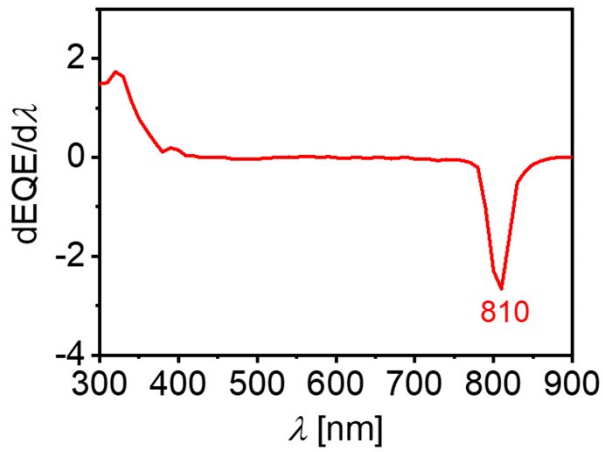

Fig. S15 First derivative spectrum of external quantum efficiency. The sharp peak at 810 nm facilitates the calculation of the

optical bandgap of the perovskite absorption layer.

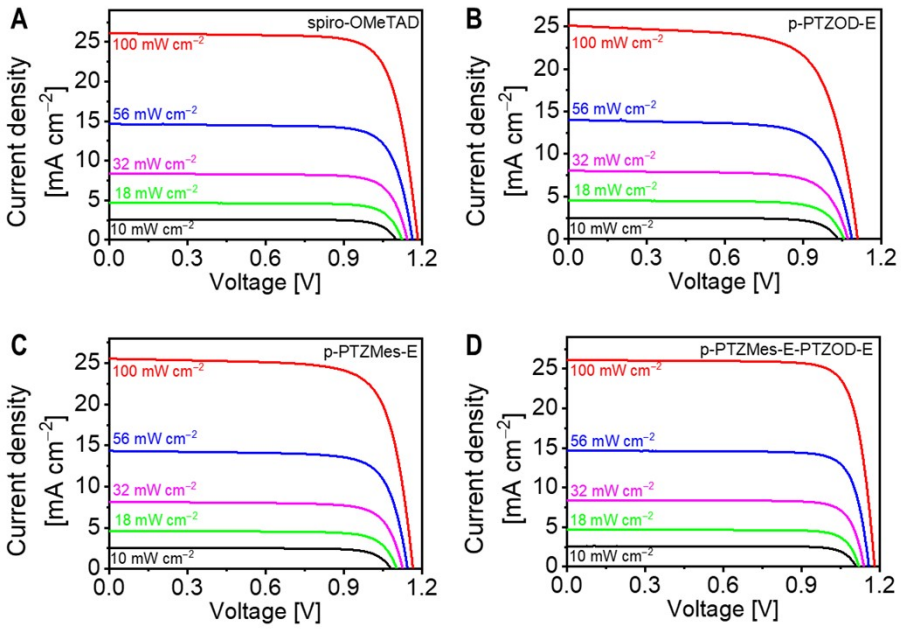

Fig. S16 (A–D) Photocurrent density–voltage curves of the cells under varying irradiance levels.

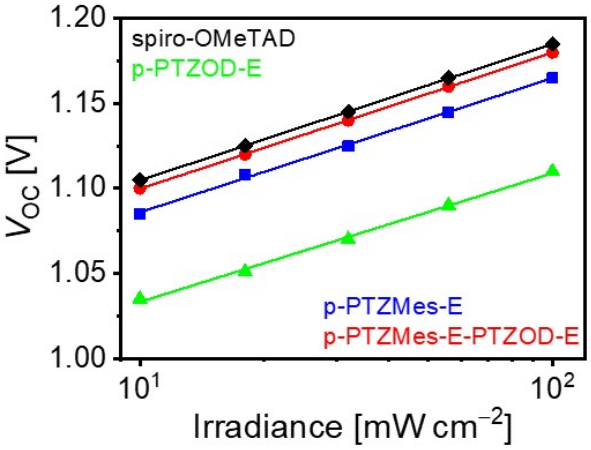

Fig. S17 Semi-logarithmic plots of open-circuit voltage (V_{OC}) versus irradiance.

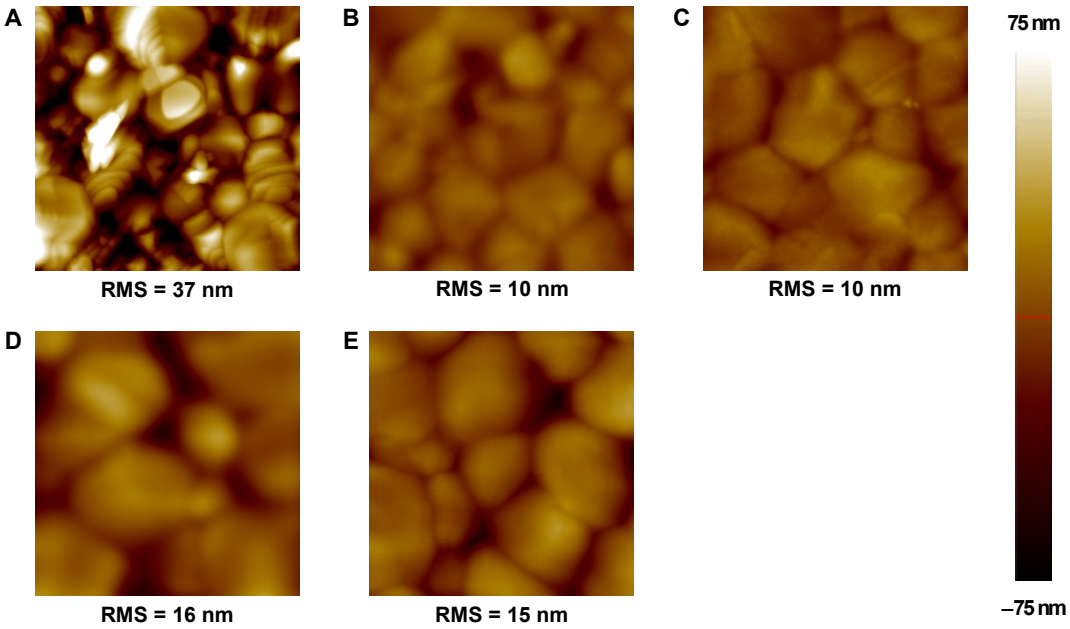

Fig. S18 Atomic force microscopy images for the sample of ITO/SnO_2/perovskite/TTI-derived layer (A) and that covered with an HTL of (B) spiro-OMeTAD, (C) p-PTZOD-E, (D) p-PTZMes-E, or (E) p-PTZMes-E-PTZOD-E. The root mean square (RMS) roughness values are shown below each image. Image size: 5 μm × 5 μm.

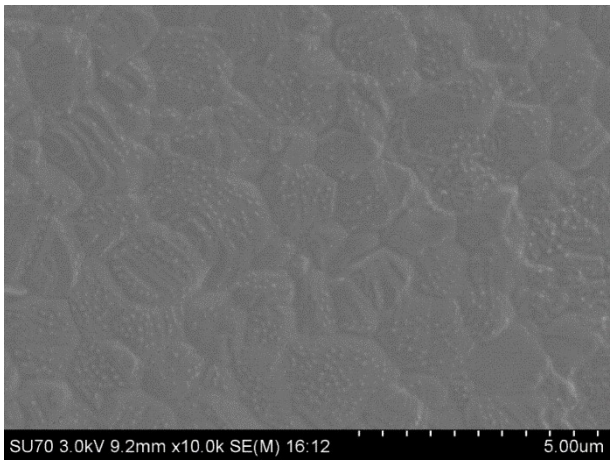

Fig. S19 Top-view scanning electron microscopy image of the $FAPbI_3$ perovskite layer in the as-prepared perovskite solar cells. The scale bar is 5 μm. Prior to imaging, the gold electrode was removed, and the hole transport layer was subsequently washed away.

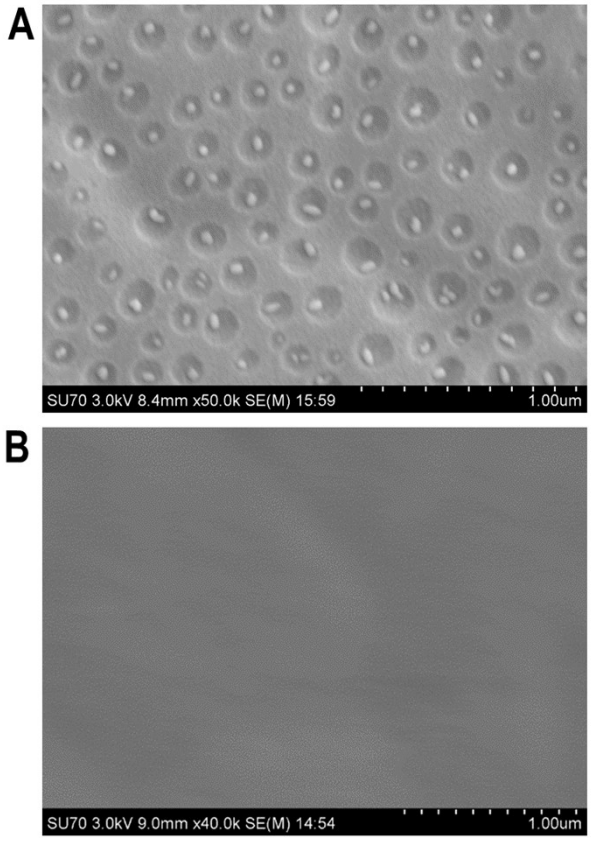

Fig. S20 (A) Scanning electron microscopy image of the p-PTZOD-E-based hole transport layer containing 15 wt% TBPH-TFSI deposited on the surface of $FAPbI_3$ perovskite film. Scale bar: 1 μm. (B) Scanning electron microscopy image of the pristine p-PTZOD-E film deposited on the surface of $FAPbI_3$ perovskite film. Scale bar: 1 μm.

Table S2. Representative photovoltaic parameters of perovskite solar cells with various hole transport layers after 1000-hour, 85 °C aging.

Cell	J_{SC} [mA cm^{-2}]	V_{OC} [V]	FF [%]	PCE [%]
spiro-OMeTAD/aged	23.08	1.110	67.7	17.3
p-PTZOD-E/aged	19.56	0.910	37.1	6.7
p-PTZMes-E/aged	24.83	1.125	73.3	20.5
p-PTZMes-E-PTZOD-E/aged	25.39	1.150	77.0	22.5

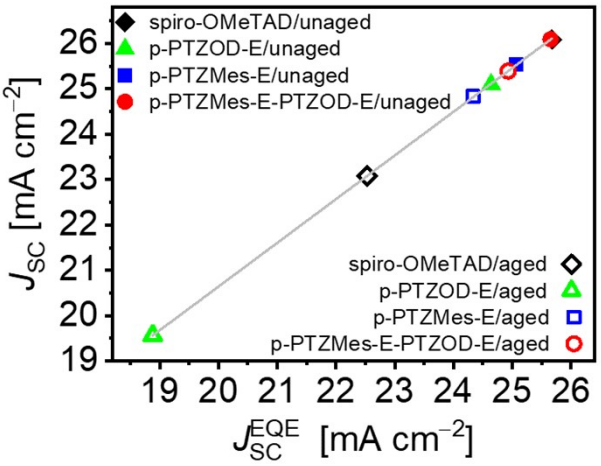

Fig. S21 The correlation between short-circuit photocurrent density derived from photocurrent density–voltage measurements (J_{SC}) and from external quantum efficiency spectra (J_{SC}^{EQE}) for unaged and 1000-hour, 85 °C aged perovskite solar cells with various hole transporting layers. A linear fit is shown by the gray line.

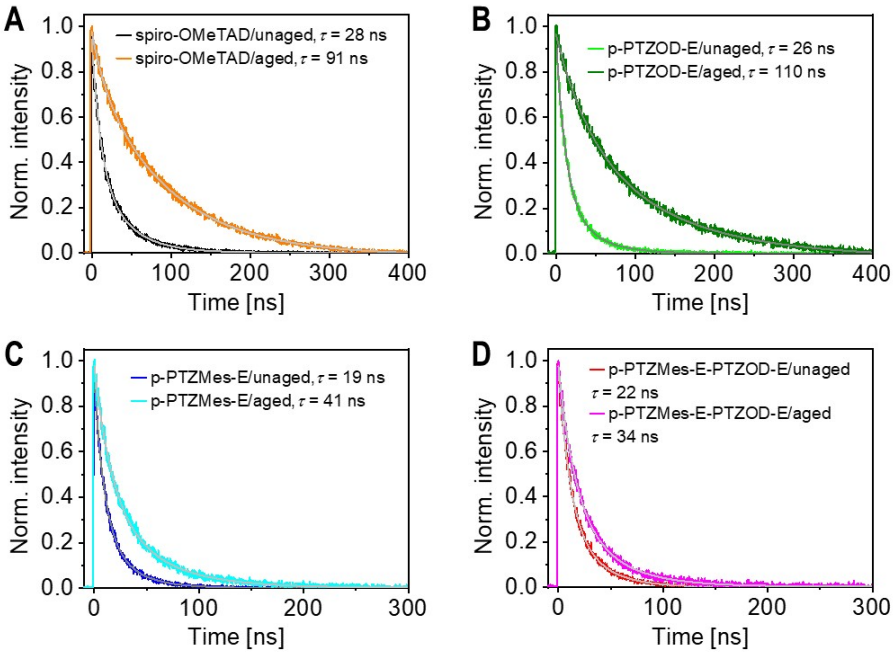

Fig. S22 (A–D) Time-resolved photoluminescence traces at 810 nm for the cells before and after 1,000-hour, 85 °C aging. The excitation wavelength used was 670 nm.

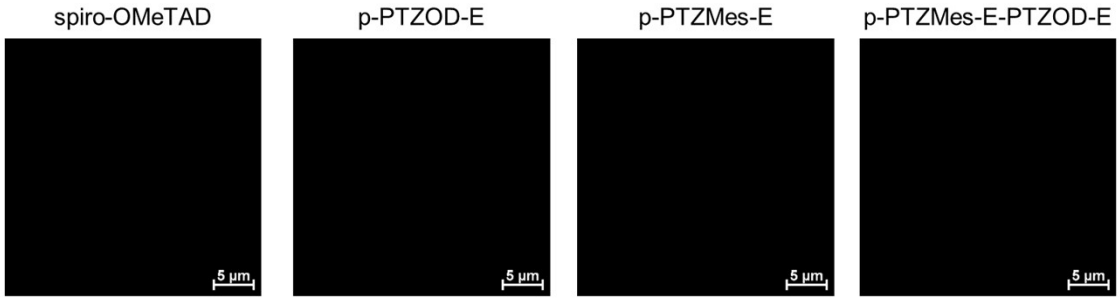

Fig. S23 Fluorescence optical microscopy images of perovskite layers in as-prepared perovskite solar cells with hole transport layers containing 15 wt% TBPH-HFSI. Scale bar: 5 µm.

4. Appendix: ^{1}H NMR spectra, ATR-FTIR spectra, UV-vis spectra, and HT-GPC analysis

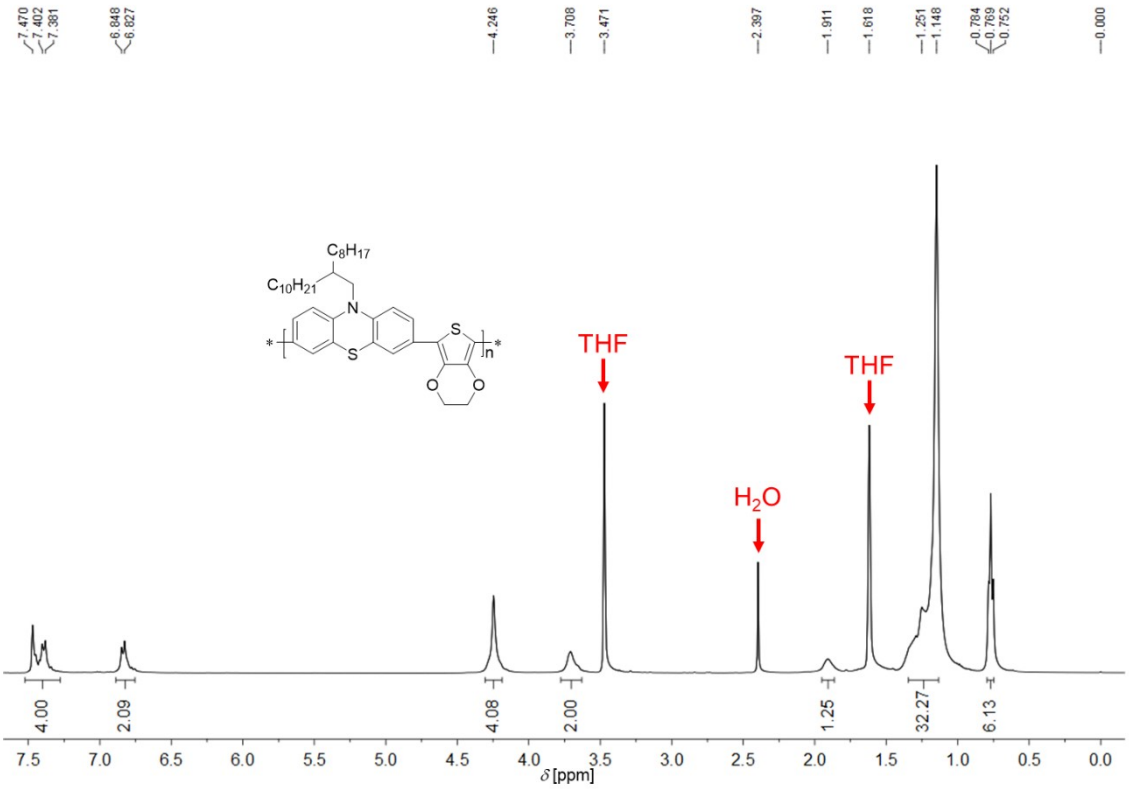

Fig. S24 ^{1}H NMR (400 MHz) spectrum of p-PTZOD-E in THF-d_8.

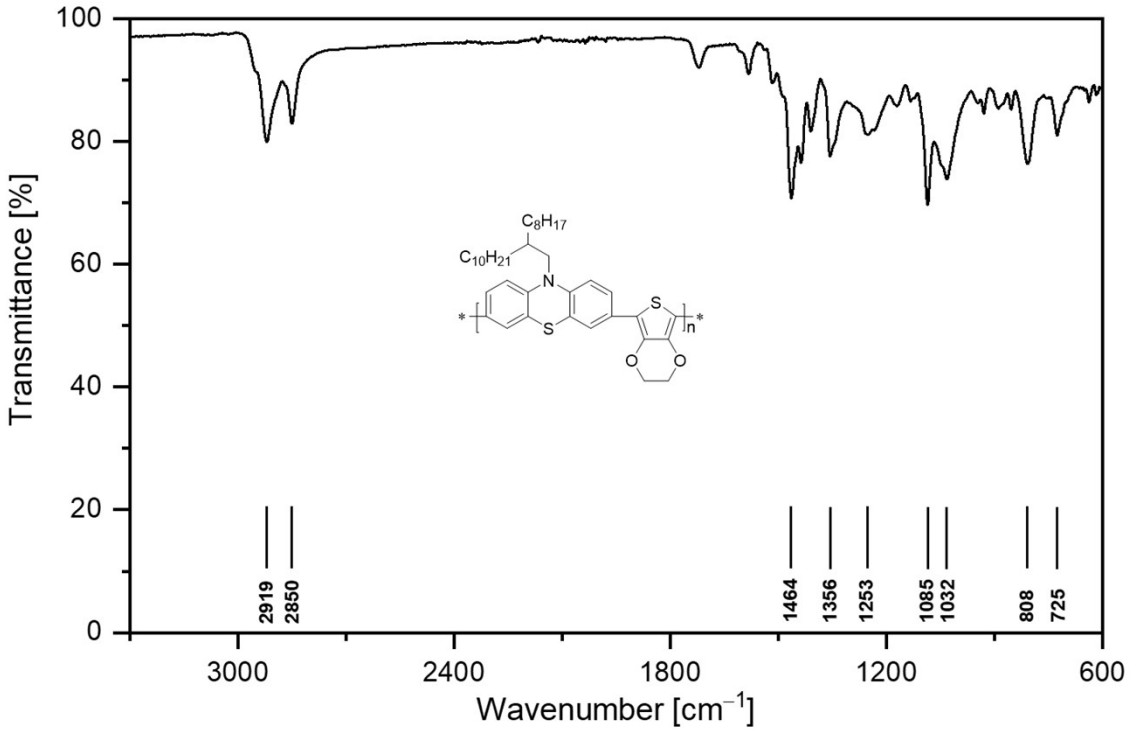

Fig. S25 ATR-FTIR spectrum of p-PTZOD-E.

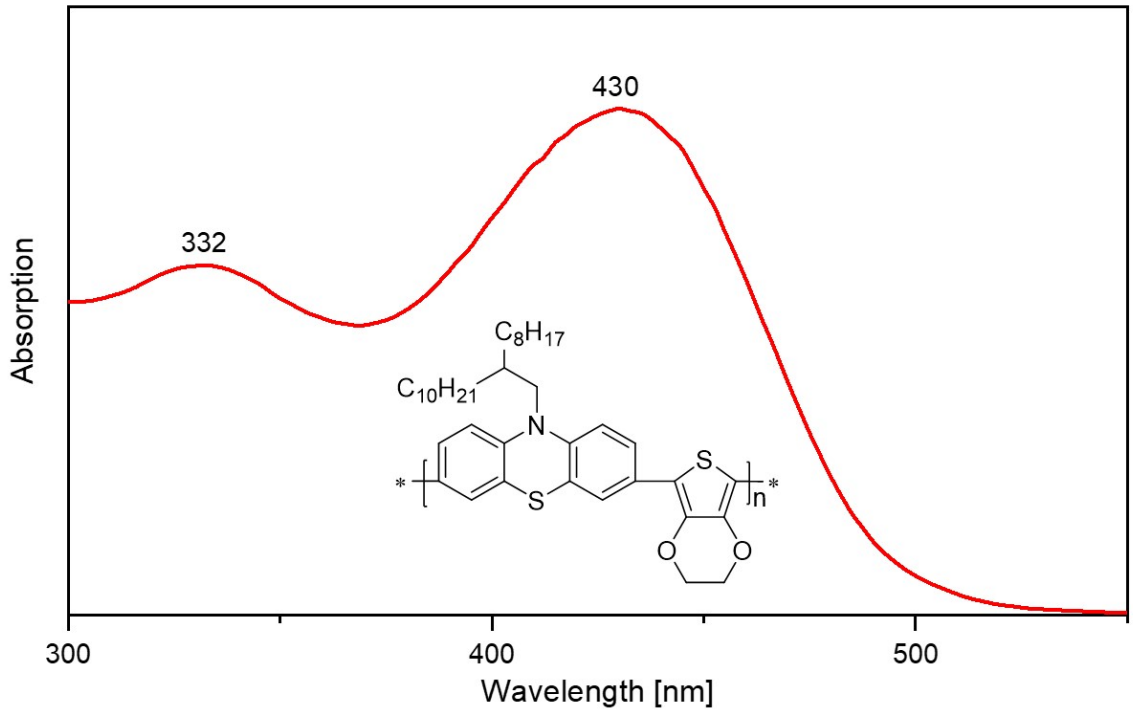

Fig. S26 UV-vis absorption spectrum of p-PTZOD-E in tetrahydrofuran.

Calibration Used: 2023/12/30 11:36:48

High Limit MW RT: 11.12 mins

High Limit MW: 5888269

K: 17.5000

Low Limit MW RT: 17.42 mins

Low Limit MW: 572

Alpha: 0.6700

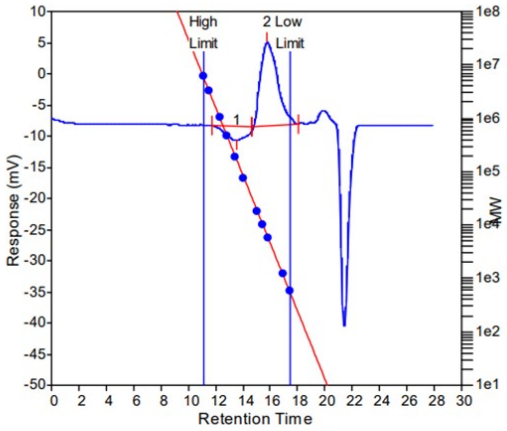

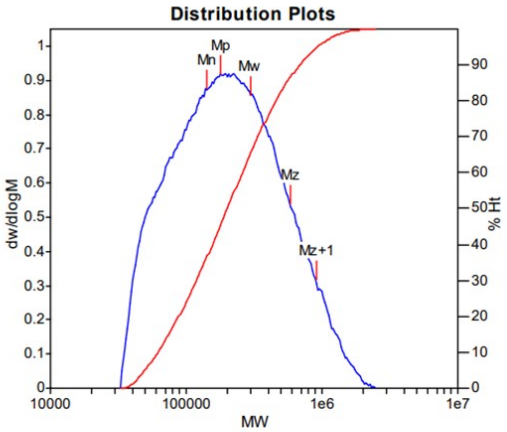

MW Averages

Peak No	Mp	Mn	Mw	Mz	Mz+1	Mv	PD
1	178673	140501	298934	586054	904593	263347	2.12763

Fig. S27 High-temperature gel permeation chromatography analysis of p-PTZOD-E.

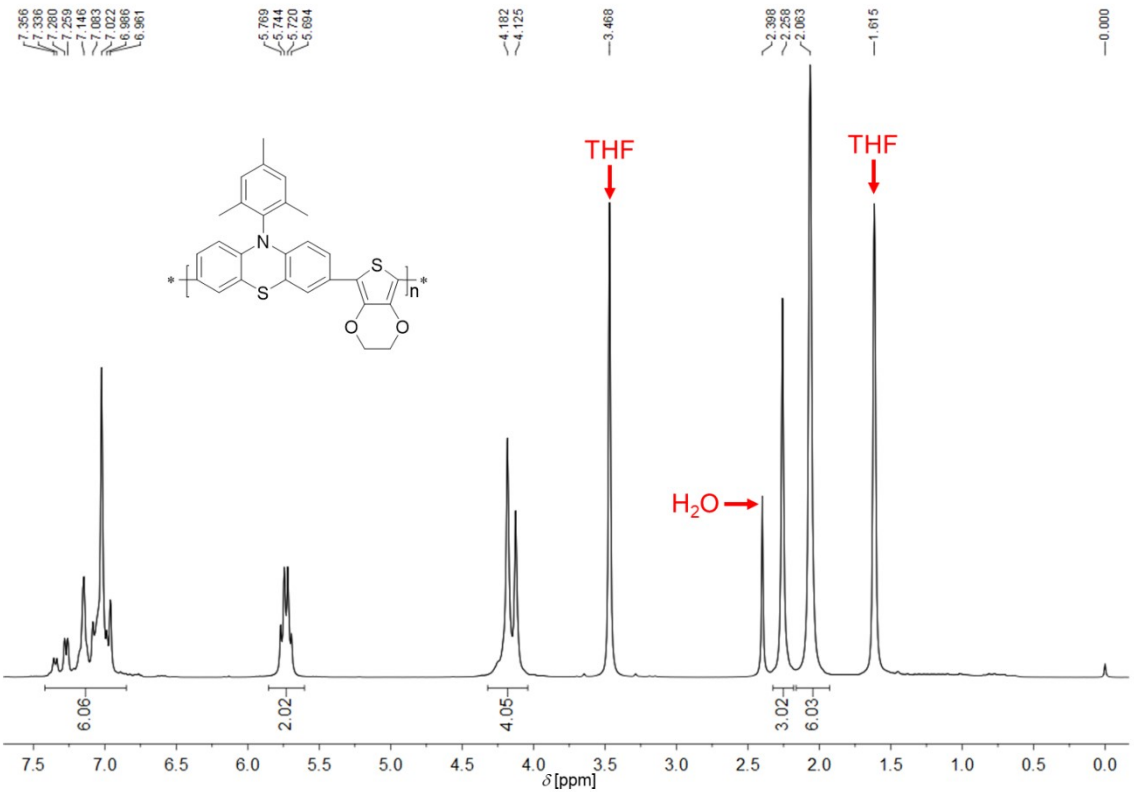

Fig. S28 ^{1}H NMR (400 MHz) spectrum of p-PTZMes-E in THF-d_8.

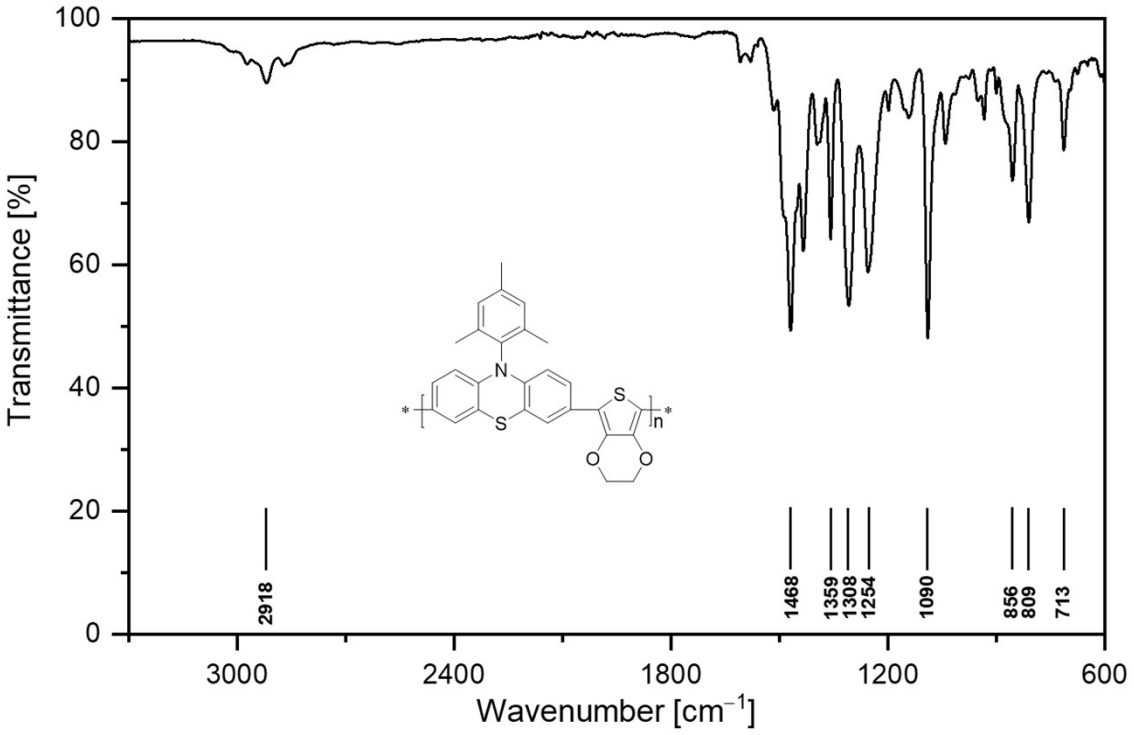

Fig. S29 ATR-FTIR spectrum of p-PTZMes-E.

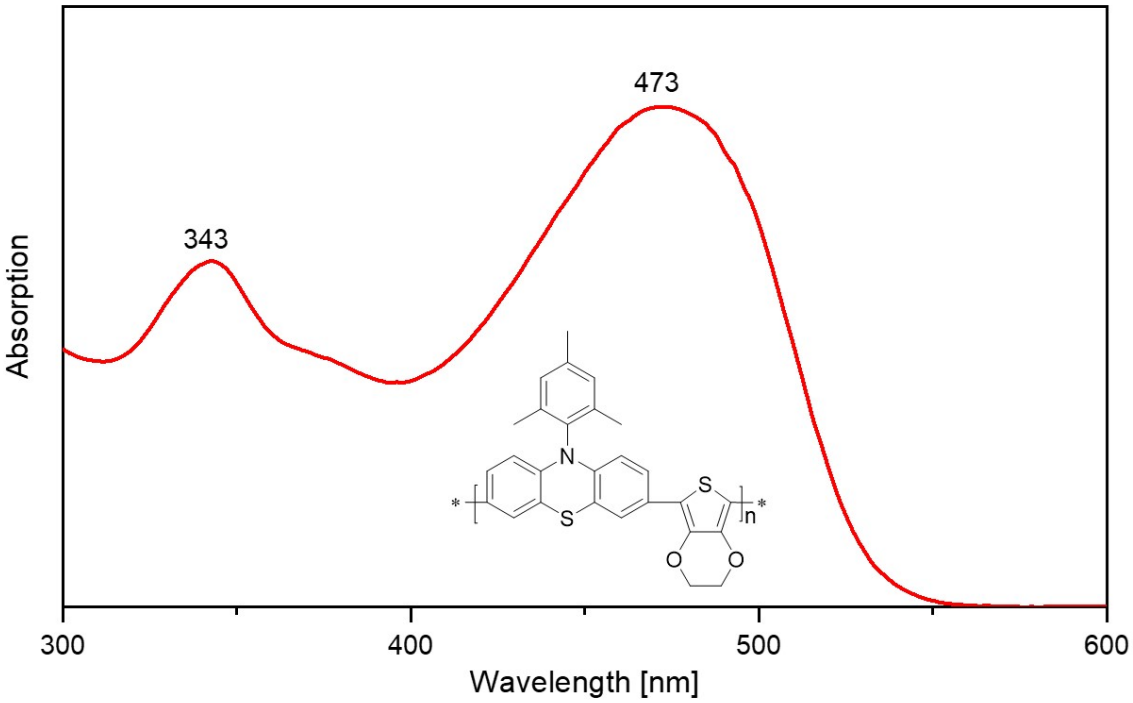

Fig. S30 UV-vis absorption spectrum of p-PTZMes-E in tetrahydrofuran.

Calibration Used: 2024/3/27 15:58:19

High Limit MW RT: 11.10 mins
High Limit MW: 5983396
K: 17.5000

Low Limit MW RT: 17.48 mins
Low Limit MW: 570
Alpha: 0.6700

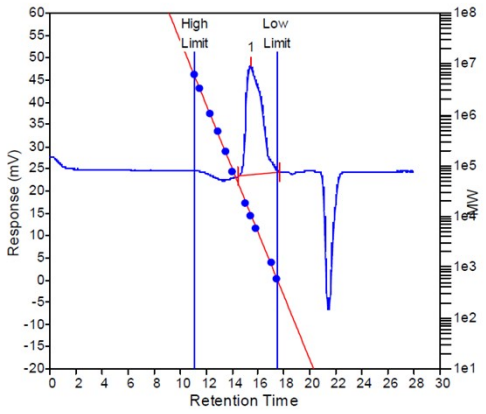

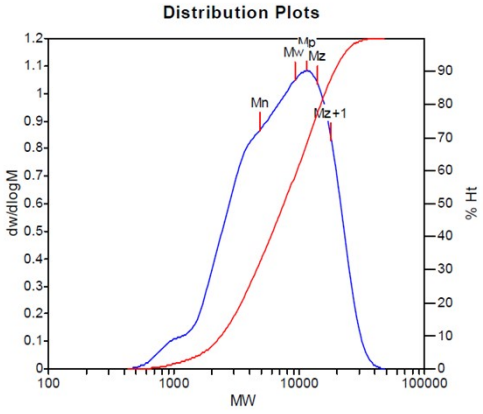

MW Averages

Peak No	Mp	Mn	Mw	Mz	Mz+1	Mv	PD
1	11432	4888	9219	13968	17981	8473	1.88605

Fig. S31 High-temperature gel permeation chromatography analysis of p-PTZMes-E.

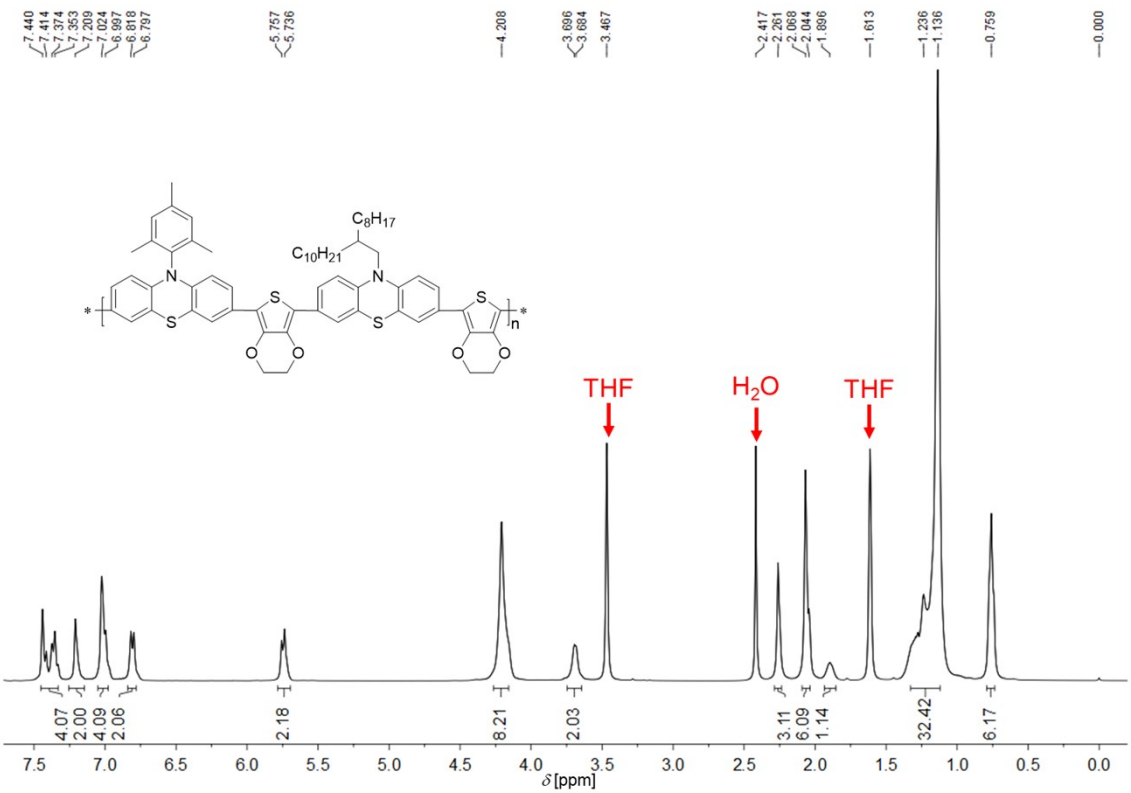

Fig. S32 ^{1}H NMR (400 MHz) spectrum of p-PTZMes-E-PTZOD-E in THF-d_8.

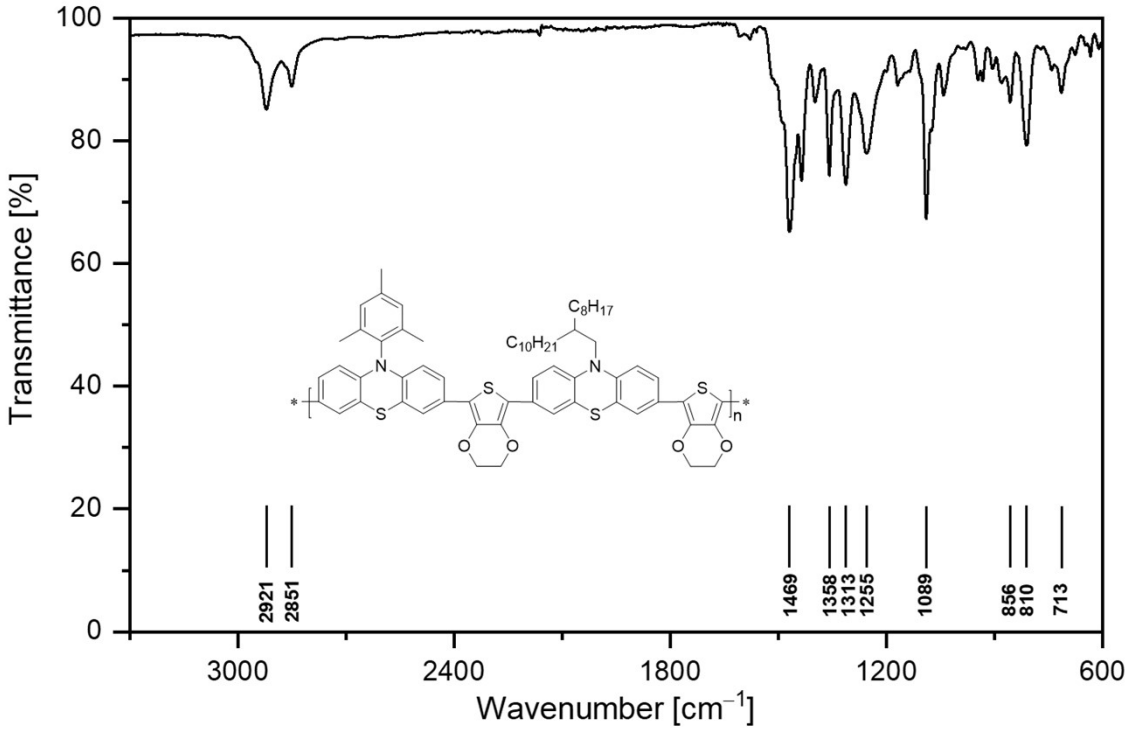

Fig. S33 ATR-FTIR spectrum of p-PTZMes-E-PTZOD-E.

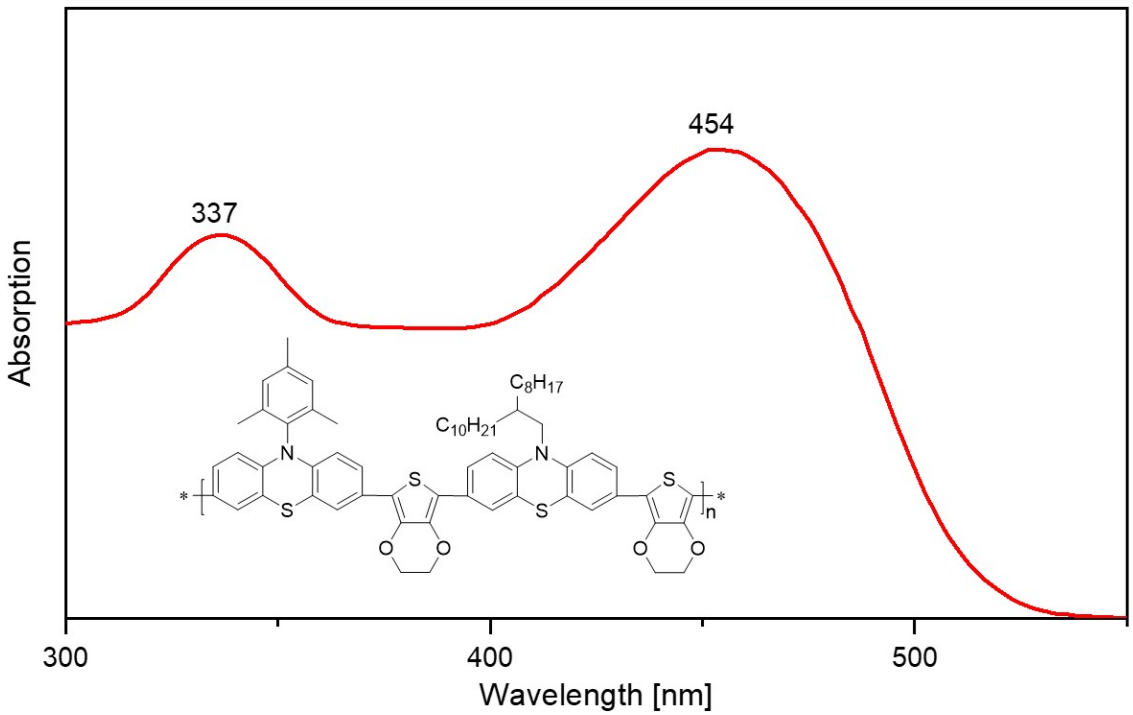

Fig. S34 UV-vis absorption spectrum of p-PTZMes-E-PTZOD-E in tetrahydrofuran.

Calibration Used: 2023/12/30 11:36:48

High Limit MW RT: 11.12 mins
High Limit MW: 5888269
K: 17.5000

Low Limit MW RT: 17.42 mins
Low Limit MW: 572
Alpha: 0.6700

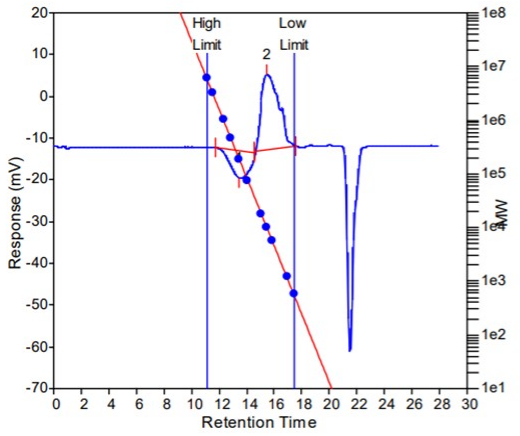

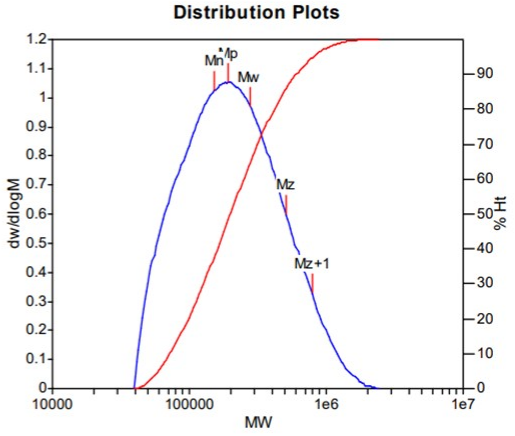

MW Averages

Peak No	Mp	Mn	Mw	Mz	Mz+1	Mv	PD
1	192266	152011	279613	506760	785134	251537	1.83943

Fig. S35 High-temperature gel permeation chromatography analysis of p-PTZMes-E-PTZOD-E.

5. References

1 H. Saito, J. Chen, J. Kuwabara, T. Yasuda and T. Kanbara, *Polym. Chem.*, 2017, **8**, 3006.

2 Y.-J. Cheng, S.-Y. Yu, S.-C. Lin, J. T. Lin, L.-Y. Chen, D.-S. Hsiu, Y. S. Wen, M. M. Lee and S.-S. Sun, *J. Mater. Chem. C*, 2016, **4**, 9499.

3 Y. Zhang, L. He, Y. Cai, J. Zhang and P. Wang, *Angew. Chem. Int. Ed.*, 2024, **63**, e202401605.

4 T. Li, Y. Zhang, M. Ren, Y. Mu, J. Zhang, Y. Yuan, M. Zhang and P. Wang, *Angew. Chem. Int. Ed.*, 2024, **63**, e202401604.

5 Y. Ren, M. Ren, X. Xie, J. Wang, Y. Cai, Y. Yuan, J. Zhang and P. Wang, *Nano Energy*, 2021, **81**, 105655.

6 Y. Zhao, F. Ma, Z. Qu, S. Yu, T. Shen, H.-X. Deng, X. Chu, X. Peng, Y. Yuan, X. Zhang and J. You, *Science*, 2022, **377**, 531.

7 Q. Jiang, Y. Zhao, X. Zhang, X. Yang, Y. Chen, Z. Chu, Q. Ye, X. Li, Z. Yin and J. You, *Nat. Photonics*, 2019, **13,** 460.

8 Y. Wei, Y. Zhang, Y. Ren, B. Zhang, Y. Yuan, J. Zhang and P. Wang, *Adv. Funct. Mater.*, 2023, **33**, 2307501.

9 C. M. Cardona, W. Li, A. E. Kaifer, D. Stockdale and G. C. Bazan, *Adv. Mater.*, 2011, **23**, 2367.

10 L. He, Y. Zhang, Y. Wei, Y. Cai, J. Zhang and P. Wang, *Matter*, 2023, **6**, 4013.